

## Article

# Optimization of Corrugated Sheet Packing Structure Based on Analysis of Falling Film Flow Characteristics

Junhua Liao <sup>1</sup>, Peng Xue <sup>1,\*</sup> , Ling Jin <sup>1</sup> , Mengjing Zhao <sup>2</sup>, Nan Zhang <sup>1</sup> and Junjie Liu <sup>3</sup>

<sup>1</sup> Beijing Key Laboratory of Green Building Environment and Energy Saving Technology, Beijing University of Technology, Beijing 100124, China; liaojunhua1111@emails.bjut.edu.cn (J.L.); jl15300215706@163.com (L.J.); zhangn@tju.edu.cn (N.Z.)

<sup>2</sup> Department of Building Services Engineering, The Hong Kong Polytechnic University, Hong Kong, China; zhaomengjing321@gmail.com

<sup>3</sup> Tianjin Key Laboratory of Indoor Air Environmental Quality Control, School of Environmental Science and Engineering, Tianjin University, Tianjin 300072, China; jjliu@tju.edu.cn

\* Correspondence: xp@bjut.edu.cn; Tel.: +86-188-1303-0116; Fax: +86-10-6739-1608 (ext. 803)

**Abstract:** The falling film flow characteristics of a liquid on the surface of corrugated sheet packing are crucial for its mass transfer performance in various industrial applications. In this study, a falling film flow experiment with laser-induced fluorescence technology was conducted to validate the flow characteristics of a falling film simulated using computational fluid dynamics (CFD). The influences of Reynolds number (Re) and the packing structure on flow characteristics were analyzed with quantitative film thickness and wetted area obtained through three-dimensional simulation. The results show that the CFD model can accurately predict the liquid falling-film flow behavior and calculate the characteristic parameters. For sinusoidal corrugated sheets, when Re reaches 500, the groove flow changes into a rivulet flow along the adjacent ripples and the wetted area is at its largest, about 0.022 m<sup>2</sup>. However, relative to the geometric area of the corrugated sheet, the wetted area can only reach 20% of the surface area, and the overall wetting performance is still poor. Triangular and trapezoidal corrugated sheets were further proposed and proved to improve the wetting area compared with the sinusoidal sheet, with maximum increases of 23% and 9%, respectively. On this basis, extensive research was carried out on the corrugation angle. The results show that a triangular corrugated sheet with a 75° corrugated angle was more conducive to the flow of the liquid film, and the wetted area was 38.8% of the surface area.

**Keywords:** corrugated sheet packing; falling film flow; laser-induced fluorescence technology; computational fluid dynamics



**Citation:** Liao, J.; Xue, P.; Jin, L.; Zhao, M.; Zhang, N.; Liu, J. Optimization of Corrugated Sheet Packing Structure Based on Analysis of Falling Film Flow Characteristics. *Sustainability* **2022**, *14*, 5861. <https://doi.org/10.3390/su14105861>

Academic Editors: Dariusz Butrymowicz and Huiming Zou

Received: 15 April 2022

Accepted: 8 May 2022

Published: 12 May 2022

**Publisher's Note:** MDPI stays neutral with regard to jurisdictional claims in published maps and institutional affiliations.



**Copyright:** © 2022 by the authors. Licensee MDPI, Basel, Switzerland. This article is an open access article distributed under the terms and conditions of the Creative Commons Attribution (CC BY) license (<https://creativecommons.org/licenses/by/4.0/>).

## 1. Introduction

Structured packing are widely used in evaporative cooling, air washers, and petroleum fractionation processes owing to their high efficiency and low pressure drop [1–3]. They are generally made of corrugated sheets arranged in a crisscross fashion with a high contact area and void fraction [4]. The inclined surface and tortuous flow channel facilitate the spread of the liquid to form a film. It is also beneficial to increase the contact time of the gas–liquid two-phase flow and promote mass transfer [5,6]. In this case, the essential flow characteristics (liquid film thickness, wetted area, liquid holdup, etc.) of the fluid in the packing system must be well understood to enhance the mass transfer efficiency [7,8]. However, this is still a challenging problem owing to the large number of factors that influence the flow behavior, such as packing structural characteristics (e.g., corrugation form and corrugation angle), surface characteristics (e.g., contact angle and roughness), solvent properties (e.g., surface tension and viscosity), and liquid load [9].

Experimental work is the traditional way to study the flow behavior of structured packing. Because of the limitation of experimental conditions in the early stage, most basic

research has mainly revealed the amplitude and phase shift of the free surface of a sinusoidal corrugated sheet, which is related to surface tension, wavelength, and direction [10,11], and the trend of wavy amplitude with changing liquid Reynolds number (Re), corrugation angle, etc. [12]. With the development of measurement technology, it has become possible to use noncontact measurement technology to measure flow field information without disturbing the system. Zhang et al. [13] used laser-induced fluorescence (LIF) technology to photograph and analyze the flow pattern of a liquid on a corrugated sheet made of plexiglass; they visualized the flow and distribution of the fluid on the corrugated sheet. In light of that research, Huang et al. [14] analyzed the influence of temperature on the falling film flow pattern on the surface of a corrugated sheet and confirmed the shrinkage of the non-isothermal falling-film flowing liquid film. Similar to LIF, ultraviolet fluorescence observation can be used to visualize the flow and has been used to analyze the flow behavior of liquids on SiC foam corrugated sheets [15]. In addition, X-ray tomography can explore the natural flow pattern of a liquid in a packed column and estimate the local and global liquid holdup and wetted area by image processing [16]. Bradtmöller et al. [17,18] used this technique to reveal the complex interdependence of liquid load and viscosity on liquid holdup in regular packings; they identified three flow modes, among which the falling film flow is generally considered the most important flow mode. The experimental study is intuitive and realistic; however, it is time consuming and cannot provide all the flow details and strict conditions actually required for the experimental setup [19,20]. During the past two decades, computational fluid dynamics (CFD) has shown significant advantages and application prospects for studying flow characteristics in structured packing [21–24]. It can reveal the nature of fluid flow phenomena, predict fluid flow behavior, and help to understand further the hydrodynamic performance of structured packing, which cannot be investigated through experiments only [25,26].

In early work, the flow trajectory of the fluid and film thickness on structured packing was usually simulated using two-dimensional (2D) CFD. Szulczewska et al. [27] initially studied corrugated packing hydrodynamics using a 2D countercurrent gas–liquid flow model. They analyzed the mechanism of droplet formation and liquid film rupture and evaluated the gas–liquid boundary area based on the thickness of the liquid film. Later, Raynal et al. [28] established a two-dimensional zigzag model of the gas–liquid flow path in structured packing based on the volume of fluid (VOF) method to estimate the liquid film thickness. The VOF method focuses on analyzing the fluid flow in the local packing unit and is suitable for microscale simulations [29].

In addition, many scholars have used this method to study the flow patterns of liquid films [30,31]. They analyzed the evolution and distribution characteristics of the liquid film over time and space and found that the liquid film tends to accumulate and form droplets, causing dry areas on corrugated sheets; reducing surface tension helps create a continuous liquid film and increases the gas–liquid contact area. However, the flow phenomenon and wetted area of the corrugated sheets as a whole cannot be captured by 2D simulations and require a three-dimensional (3D) simulation for investigation [32].

With the rapid development of computers, various 3D studies have been conducted. Ataki and Bart [33] established a VOF model of the local unit of Rombopak packing to describe the influence of liquid load and liquid properties on wetting. The results showed that the wettability increased with an increase in liquid viscosity and load. Similarly, Haroun et al. [34] simulated the flow of liquid on a corrugated sheet and found that the degree of wetting of the corrugated sheet increases as the liquid load increases and the solid–liquid contact angle decreases. Shojaee et al. [35] calculated the interface area using liquid holdup and the average film thickness, and found that the interfacial area appeared to be effectively equivalent to the wetted area. In addition, the liquid inlet location and size also have important effects on wetting behavior. Subramanian et al. [36] used the VOF method to examine both rivulet flow on a single corrugated sheet with a single liquid inlet and wetting behavior on two layers of corrugated sheets with multiple liquid inlets. It was found that a minor change in the position of the inlet distributors considerably changes the wetting area

and flow direction of the liquid. On this basis, Singh et al. [37] considered the influence of the corrugation angle  $\beta$  and believed that a  $\beta$  of  $45^\circ$  was more conducive to the flow of the rivulet on the corrugated sheet. Because of the liquid inlet size setting, only a single rivulet flow was analyzed, and it was not possible to describe the wetting situation on the entire plate. The effects of packing surface characteristics, liquid properties, and loads on the flow characteristics have been studied and reported in the literature. However, these simulations were restricted to small computational domains because of limited computational resources; industrial-scale simulations were almost impossible. Extensive investigation of the effect of packing structural characteristics on flow characteristics is lacking.

In this study, a falling film–flow experimental platform was built, and the CFD method was used to explore the phenomenon of liquid falling film flow on corrugated sheets of an industrial application scale. An LIF experiment was conducted to validate the 3D simulation of the falling film flow, and the influence of Re and packing structure on the flow characteristics of the falling film was further analyzed. The results have guiding significance and practical application value for the optimization of corrugated sheet structures, the control of liquid film thickness, and the maximization of wetting.

## 2. Methodology

Due to the complex structure of the corrugated sheet packing, it is almost impossible to obtain its flow characteristic parameters through experiment, and the flat plate form is generally regarded as its most simplified unit [38]. Therefore, this study firstly verifies the effectiveness of CFD simulation on the flat plate through LIF experiments, and 3D model simulation was used to study the detailed flow behavior of the corrugated sheet and its influencing factors.

### 2.1. Experimental Setup

#### 2.1.1. Experimental Device

The falling film–flow experimental bench consisted of a structure platform, water circulation system, and data acquisition system, as shown in Figure 1. The structure platform was made of acrylic material for convenient observation, and all detailed information for the experiment is listed in Table 1.

**Table 1.** Description of experimental equipment.

Equipment	Model/Material	Usage/Size Description
Circulating water tank	Acrylic	Capacity 15 L
Rotameter	NBDC	0~400 m <sup>3</sup> /(m <sup>2</sup> ·h)
Water pump	CRUNDFOS	Head 5 m
Conical water distribution device	Acrylic	Evenly distributes water on the working surface
Flat plate	Stainless steel	275 × 310 × 1 mm
Rhodamine B	Powder	1 mg/L
Laser	PSU-H-LED	Service power
Camera	GX85	Frame rate 25 fps
Electronic scale	METTLER TOLEDO	Range 0.01–4100 g

A tapered water distribution device and an overflow plate were placed at the top of the structure platform to achieve a uniform flow of liquid on the inlet surface. The middle of the platform was a falling film flow section with a flat plate placed close to the wall; circulating water was provided by a water tank placed at the bottom of the platform during the experiment. The liquid in the water tank was transported by a water pump through valves, rotameters, water distribution devices, and overflow plates, forming a uniform liquid film on the surface of the flat plate. It finally flowed back into the bottom water tank. In the data acquisition system, the laser emitted light to irradiate the surface of the flat plate through the structural platform, and a camera was used to capture the fluorescence reflected by the liquid film from the side simultaneously.

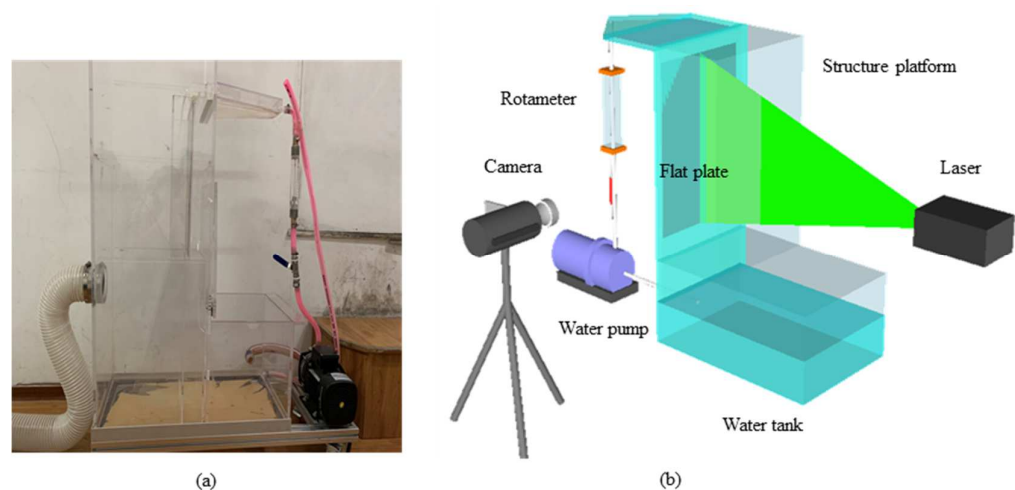


**Figure 1.** Falling film-flow experimental platform: (a) experimental setup and (b) experimental system.

### 2.1.2. Experimental Principles and Steps

To visualize the flow behavior, LIF technology was used in this experiment. LIF technology involves mixing rhodamine B in the liquid so that the liquid can reflect fluorescence under irradiation with a specific wavelength of laser light [39]. The flow field information was recorded using image-processing technology, and the average liquid film thickness was obtained. The following operations were performed to ensure experimental accuracy.

- (1) The rhodamine B solution was dropped on a plate to determine the fluorescence color rendering. It was then placed in a dark room, and the laser hit the droplets on the plate vertically to prove that the boundary of the liquid film was obvious after fluorescence, as shown in Figure 2a;
- (2) A two-stage overflow device, presented in Figure 2b, was set between the cone water distribution device and the falling film flow section to guarantee a uniform flow on the liquid inlet surface and ignore the influence of airflow in the channel;
- (3) The liquid load was controlled to be  $180\text{--}240\text{ m}^3/(\text{m}^2\cdot\text{h})$  after experimental debugging to prevent the small liquid load from easily forming dry areas on the plate and, at the same time, to avoid splashing droplets during the falling film flow process with a large liquid load;
- (4) The area  $165\text{--}305\text{ mm}$  below the plate was determined to be the shooting area, which is the real height  $H_{\text{real}}$  of the image, whereas the other areas were treated with shading, as shown in Figure 2c.

Four groups of working conditions of  $180$ ,  $200$ ,  $220$ , and  $240\text{ m}^3/(\text{m}^2\cdot\text{h})$  were used in the experiment. Each group of working conditions was taken continuously for  $10\text{ s}$  at a frame rate of  $25\text{ fps}$ ;  $1000$  images were obtained.

### 2.1.3. Image Data Processing

Python was used to process the original image and calculate the liquid film thickness, as shown in Figure 3a–c. The boundary of the liquid film was first marked in the image, and the obvious noise of the image was removed by gray-scale noise reduction. The real height  $H_{\text{real}}$  and height pixels of the image ( $N = 2496$ ) were compared to obtain the unit pixel width, which can be expressed as  $d = H_{\text{real}}/N$ . The width of a single pixel in the image at the position of the liquid film in different images was considered to be the same because the relative position of the camera and the photographed object remains unchanged; the unit pixel width ( $d = 0.06\text{ mm}$ ) was treated as the basis of the true width. In this case, the number of pixels,  $m$ , between the horizontal boundaries of the liquid film was extracted to obtain the average liquid film thickness  $\delta = m \times d$  under four working conditions, and the liquid film thickness in a whole second is the average value of the  $25$ -image data in that

second. Finally, the maximum value of the relative uncertainty [40] of the experiment is calculated to be 4.8%, indicating that the experimental results are reliable.

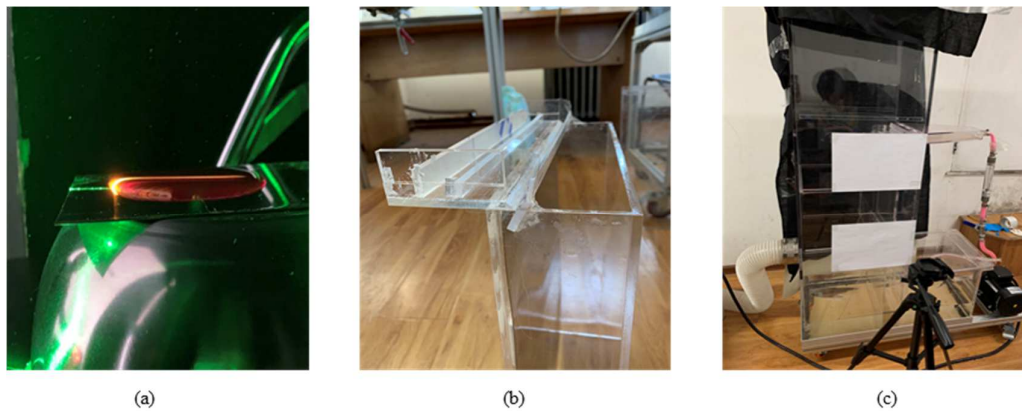


**Figure 2.** Experimental operations: (a) fluorescence color rendering judgment, (b) two-stage overflow device, and (c) shading and shooting area determination.

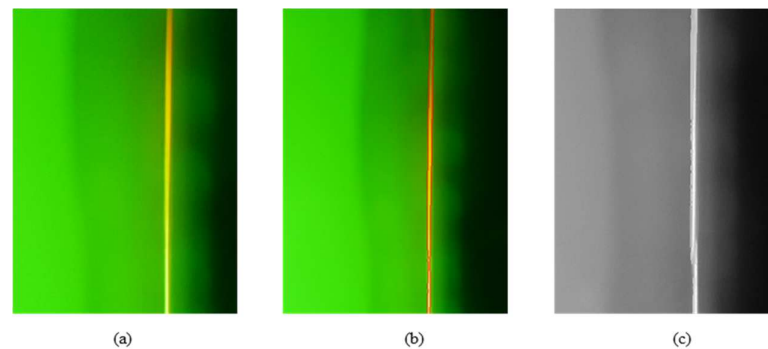


**Figure 3.** Image Processing: (a) the original image, (b) boundary labeling, and (c) grayscale noise reduction.

## 2.2. Simulation Setup

### 2.2.1. Physical Model

Based on the falling film flow experiment of the flat plate, a 3D CFD model, as shown in Figure 4a, was established using SOLIDWORKS software. The flat plate was made of metal, and the wall was set as a nonslip wall, where the inlet boundary was set as the speed inlet, and the outlet boundary was set as the pressure outlet. The physical model was meshed using the ANSYS WORKBENCH software. To ensure the accuracy of the calculation at the wall and the accurate capture of the gas–liquid interface, the grid used advanced size control, and the liquid-phase flow area near the wall was densified, as shown in Figure 4b. After the grid independence test, the number of CFD model grids was determined to be 606,760.

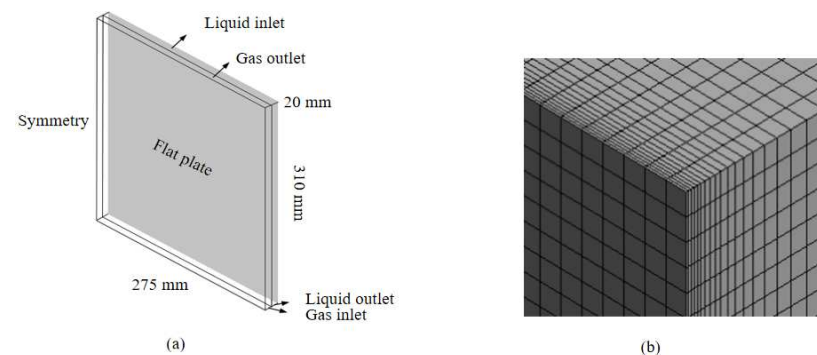


**Figure 4.** Physical model diagram: (a) physical model and (b) meshing near the wall.

In addition, according to the BZ 500 corrugated sheet structure on the market, as shown in Figure 5a, a sinusoidal corrugated sheet, as shown in Figure 5b, was established with the same length and width as the flat plate. To optimize the packing structure further, triangular and trapezoidal corrugated sheets were established—see Figure 5c,d. The boundary conditions of the corrugated sheet model are the same as the flat plate, and the detailed information of the model is shown in Table 2. For each type of corrugated sheet, 35 cases were investigated under the dual variables of  $Re$  (250, 310, 370, 430, 500, 560, and 620) and corrugation angle ( $15^\circ$ ,  $30^\circ$ ,  $45^\circ$ ,  $60^\circ$ , and  $75^\circ$ ).

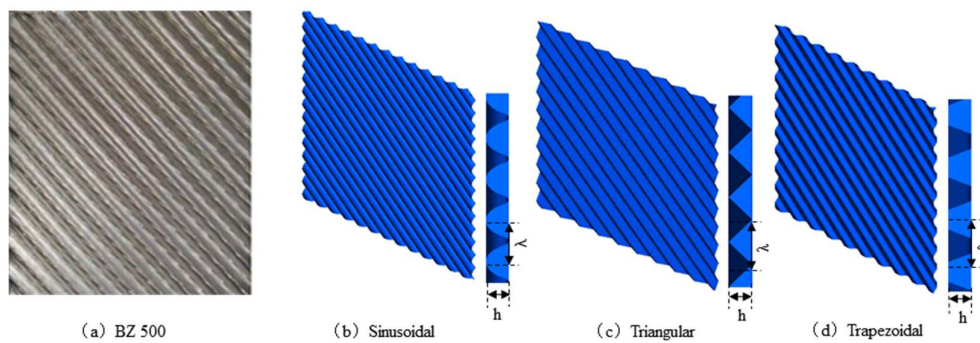


**Figure 5.** Actual corrugated sheet and corrugated sheet model: (a) BZ 500 type packing, (b) sinusoidal, (c) triangular, and (d) trapezoidal.

**Table 2.** Details of the model.

Corrugated Sheet Type	Corrugation Angle $\beta$ ( $^\circ$ )	Number of Grids after Verification	Corrugation Height, $h$ (mm)	Corrugation Base Length, $\lambda$ (mm)	Surface Area, $S_b$ ( $m^2$ )
Sinusoidal corrugated sheet	15	5,180,599	6	20.8	0.11050
	30	5,243,963			
	45	5,214,086			
	60	5,242,488			
	75	5,188,882			
Triangular corrugated sheet	15	4,303,212	6	20.8	0.09520
	30	4,305,034			
	45	4,370,668			
	60	4,267,153			
	75	4,394,006			
Trapezoidal corrugated sheet	15	4,668,025	6	20.8	0.10662
	30	4,618,415			
	45	4,632,527			
	60	4,628,643			
	75	4,690,183			

### 2.2.2. Mathematical Model

Falling film flow can be classified as a gas–liquid two-phase stratified flow, and the VOF model [41] can be used to describe the gas–liquid interface flow accurately. The tracking of the phase interface is achieved by solving the continuity equation of a certain phase  $\alpha$  in each calculation unit [42–44]. The velocity and pressure of the model satisfies the continuity equation and the classic fluid structure Navier–Stokes equation, and the surface tension force is computed using a continuous surface force model [45].

In the experiment, the actual wetting condition of the plate could not be photographed owing to the acrylic cover; hence, the Delft [46] model was used to validate the effective area ratio calculated by CFD. The Delft model does not require specific packing parameters,

and it only distinguishes between holes and nonholes; therefore, it is suitable for flat plate calculations. The calculation formula is

$$\frac{\alpha_e}{\alpha_p} = (1 - \Omega) \left\{ 1 - \exp \left[ -1.45 \left( \frac{0.075}{\sigma} \right)^{0.75} \right] Re_L^{0.1} Fr^{-0.05} We_L^{0.2} \right\} \quad (1)$$

where

$$Re_L = \frac{\rho_L u_L}{\alpha_p \mu_L} \quad (2)$$

$$We_L = \frac{\rho_L u_L^2}{\alpha_p \sigma} \quad (3)$$

$$Fr_L = \frac{u_L^2 \alpha_p}{g} \quad (4)$$

Here,  $a_e/\alpha_p$  is the effective area ratio,  $a_e$  is the effective interfacial area ( $\text{m}^2/\text{m}^3$ ),  $\alpha_p$  is the specific surface area of the packing ( $\text{m}^2/\text{m}^3$ ), and  $\Omega$  is the ratio of the surface area of open pores to the specific surface area. For flat plates,  $\Omega = 0$ .  $Re_L$ ,  $We_L$ , and  $Fr_L$  are the Reynolds number, Weber number, and Froude number, respectively. The Reynolds number represents the ratio of inertial force to viscous force, which can reflect the influence of the inertial force of the initial velocity of the liquid and the viscous force between the liquid and the corrugated sheet; it is used to describe different working conditions. The corresponding range of liquid load and Re in this study is shown in Table 3.

**Table 3.** Details of the liquid loads and Reynolds numbers presented in this work.

liquid load ( $\text{m}^3/(\text{m}^2 \cdot \text{h})$ )	180	200	220	240	250	300	350	400	450	500
Re	220	250	270	300	310	370	430	500	560	620

### 2.2.3. Simulation Settings

Simulations of the unsteady state of the falling film flow of the flat plate and corrugated sheets were performed using ANSYS FLUENT. The simulation process is under normal temperature conditions, and the temperature field and mass transfer were ignored. The gas phase was air, the initial velocity was zero, and the liquid phase was water. The effect of rhodamine B on the viscosity in the experiment was ignored [47]. The solid–liquid contact angles of the flat plate and corrugated sheets were set as  $59^\circ$  and  $57^\circ$ , respectively [48]. During the solution process, FLUENT adopts a pressure solver, and the VOF model uses an implicit format to track the gas–liquid interface effectively. The corrugated on the packing surface has a dramatic impact on the flow, and there are turbulent areas in the liquid falling film flow process. Therefore, after a series of debugging and verification, the turbulence model adopts the standard k- $\epsilon$  model. To improve the calculation accuracy and save time, the pressure implicit with splitting of operators (PISO) algorithm was used for the pressure–velocity coupling calculation of the flow field, and second-order upwind schemes were used for the momentum, turbulent kinetic energy, and turbulent energy dissipation equations. The simulation time step was set to  $10^{-3}$ , and the number of iteration steps was set to 10,000. At the beginning of the calculation, the gas phase filled the entire model—that is, the volume fraction of the gas phase was  $\alpha_g = 1$ , and the volume fraction of the liquid phase was  $\alpha_l = 0$ .

## 3. Results

### 3.1. CFD Model Validation

#### 3.1.1. Average Liquid Film Thickness Prediction

The thickness of the liquid film is an important parameter for evaluating the hydrodynamic performance and mass transfer capacity of the falling film flow on corrugated sheets

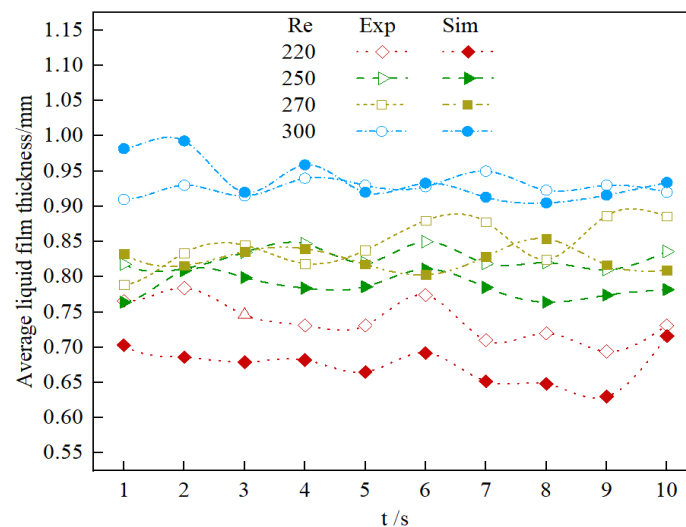
of packing. The average liquid film thickness extracted by the CFD-POST postprocessing software in the plate height range from 165 to 305 mm was compared with the experimental results to validate the accuracy of the CFD model.

Figure 6 shows the variation in the average liquid film thickness with the flow time under the four working conditions of the experiment and CFD model. The figure shows that the average liquid film thickness of the flat falling film flow is positively correlated with the Re. The larger the Re, the greater is the average liquid film thickness. The error between the experimental and simulation results can be calculated according to the normalized mean bias error (NMBE) and the coefficient of variation of the root-mean-square error (CVRMSE) in the ASHRAE standard [49]:

$$NMBE = \frac{\sum_{i=1}^n (y_i - \hat{y}_i)}{(n-1) \times \bar{y}} \times 100 \quad (5)$$

$$CVRMSE = \frac{\sqrt{\sum_{i=1}^n (y_i - \hat{y}_i)^2 / (n-1)}}{\bar{y}} \times 100 \quad (6)$$

Here,  $y_i$  and  $\hat{y}_i$  are the average liquid film thicknesses obtained by the experiment and simulation, respectively,  $\bar{y}$  is the average value of the experiment, and  $n$  is the number of samples. The errors of the two under the four working conditions are 10% and 10%, 6% and 6%, 3% and 6%, and 1% and 4%, respectively, which are far less than 15% and meet the standard requirements. This error may result from volatility and randomness in the liquid flow process. However, the simulation values are quite consistent with the experimental values in most cases; therefore, the CFD model can accurately calculate the average liquid film thickness in the falling film flow process.



**Figure 6.** Average film thickness validation.

### 3.1.2. Effective Area Ratio Validation

The wetted area refers to the area that the actual liquid phase covers on the surface of the plate. According to the experimental results, it is considered that the area where the liquid volume fraction  $\alpha$  of the plate wall surface in the CFD model is greater than or equal to 0.2 is the wetting area. The ratio of the effective area is calculated by

$$\frac{\alpha_e}{\alpha_p} = \frac{S_w}{S_b} \quad (7)$$

where  $S_w$  is the wetted area of the plate and  $S_b$  is the surface area of the plate.

CFD shows the wetting situation of the plate after the flow reaches the pseudo-steady state under different  $Re$ , as shown in Figure 7a–d, in which red represents the liquid and blue represents the wall of the plate. Under the action of a certain initial velocity and gravity, the liquid flows vertically downward along the wall in a uniform film-like form. Because viscous force and surface tension are present, the liquid film gradually shrinks inward during its downward flow and forms multiple rivulets on the lower part of the plate, resulting in dry areas, as shown in Figure 7a,b. As the  $Re$  increases, the liquid film almost completely covers the wall of the plate, as shown in Figure 7c,d.

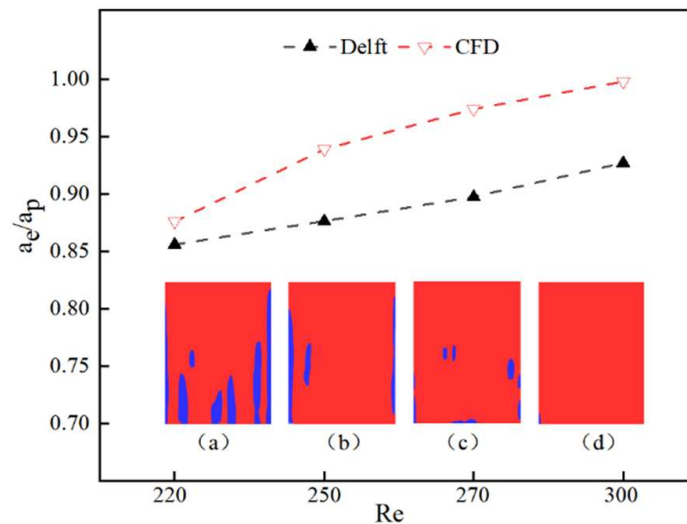


**Figure 7.** Validation of the effective area ratio, with the wetting situation of the plate under different  $Re$ : (a) 220, (b) 250, (c) 270, and (d) 300.

The effective area ratio predicted by the CFD model was compared with the results calculated using the Delft empirical model. Figure 7 reveals that the  $a_e/\alpha_p$  calculated by the CFD model is higher than the value calculated by the Delft model under different working conditions. This is because the CFD model in this study and the Delft model have different ways of solving  $a_e/\alpha_p$ . The numerical simulation process integrates the volume fraction of water through the CFD-POST postprocessing software to obtain the wetted area, whereas the Delft model is an empirical formula derived from a large amount of experimental data. However, the normalized mean bias error and root-mean-square error values of the two methods are 9% and 8%, respectively, which are within the acceptable range. The results show that the CFD model can predict the wetted area of the falling film flow process more accurately.

### 3.2. Hydrodynamic Performance of the Liquid Falling Film Flow on Corrugated Sheet Packings

#### 3.2.1. Transient Flow Development

Because a corrugated sheet has a large number of inclined wavy structures, the liquid does not flow uniformly on the surface of the falling film, and the liquid flow information on its surface cannot be photographed by the LIF method. Corrugated sheets and flat plates are only different in structure. The other conditions, such as material properties, boundary conditions, and simulation settings, are the same; hence, the CFD model is still treated as an accurate method for investigation. However, as opposed to the flat plate, it is impossible to evaluate the liquid film thickness of the entire corrugated sheet using only the value of the liquid film thickness on a certain section; hence, the average liquid film thickness is defined by the liquid volume  $V_L$  and the wetted area  $S_w$  as  $\delta_{av} = V_L/S_w$  [4]. Figure 8 shows the gradual flow of the liquid on the corrugated sheet when the  $Re$  is 250.

In Figure 8a,b, the initial liquid flows uniformly from the liquid phase inlet in the form of a film. Under the action of gravity and surface tension, the liquid on the wave crest gradually converges into the wave trough. The liquid in the wave trough is squeezed and

gradually flows downward across the adjacent corrugations, and a large-scale rivulet phenomenon forms on the corrugated sheet. During the flow, the liquid gradually overcomes the resistance in the trough channel, the phenomenon of rivulet flow weakens, and water droplets, small rivulets, rivulet breaks, etc. form, as shown in Figure 8c. In Figure 8d,e, the flow reaches a pseudo-steady state for approximately 1 s. The liquid forms a regular flow in the trough along the inclined direction of the corrugation, and the groove flow becomes the main flow form. The area covered by the liquid film of the corrugated sheet is significantly reduced compared with that of the rivulet.

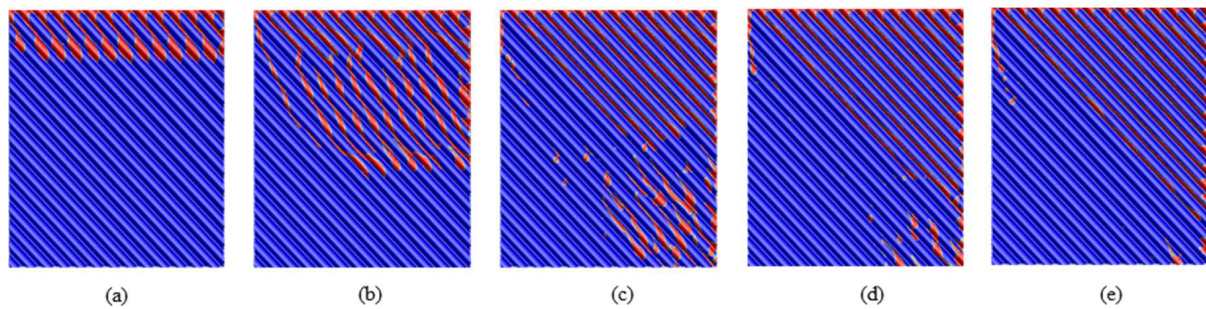


**Figure 8.** Transient flow of liquid at: (a)  $t = 0.2$  s, (b)  $t = 0.4$  s, (c)  $t = 0.6$  s, (d)  $t = 0.8$  s, and (e)  $t = 1$  s.

### 3.2.2. Effect of Re on Hydrodynamic Performance

The Re affects the liquid flow behavior and liquid phase distribution to a certain extent. A large-scale study on the Re was carried out, and the results are shown in Figure 9.

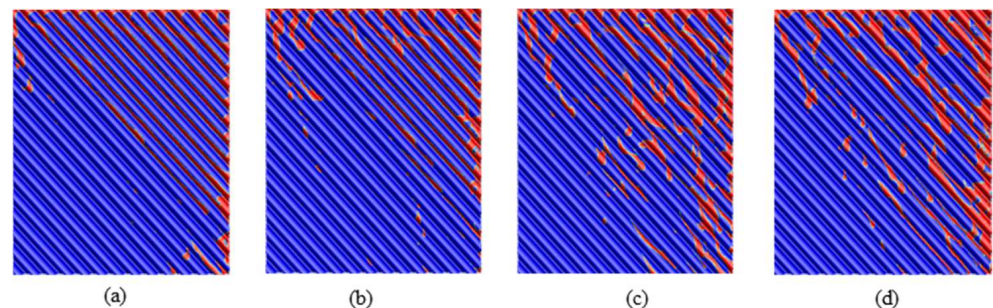


**Figure 9.** Wetting of the corrugated sheet at  $t = 1$  s under different Re: (a) 370, (b) 430, (c) 500, and (d) 620.

Figure 9a shows that when the Re is 370, the liquid still flows in the trough in the form of a groove flow. The increase in Re causes the groove flow width to increase compared with when Re is 250. When the Re is 430, the initial momentum of the liquid increases so that a rivulet begins to appear at the inlet, but the rivulet is hindered by ripples in the downward flow process, and the rivulet gradually turns into a groove flow, as shown in Figure 9b. In Figure 9c, the Re reaches 500, and the momentum of the liquid is sufficient to overcome the resistance between the ripples. At this time, the rivulet on the corrugated sheet occupies the main position. However, when the Re is further increased to 620, the collision between the falling liquid and ripples increases, causing a loss of momentum, as shown in Figure 9d. As a result, the liquid falls off the surface of the corrugated sheet, and the area of the rivulet is significantly reduced. Figure 10 summarizes the average liquid film thickness and wetted area of the corrugated sheet under different Re values.

When the Re values are 250, 310, and 370, the liquid mainly flows in the form of a groove flow. The increase in Re causes the average liquid film thickness in the trough to increase gradually, whereas the wetted area does not change significantly. When the Re is increased to 430, the rivulet phenomenon appears, and the wetted area is increased. However, in the downward flow process, the rivulet is hindered by ripples and gradually turns into a groove flow, and the average liquid film thickness reaches the maximum value, which is about 2.47 mm. When the Re is increased to 500, the rivulet phenomenon appears,

and the wetted area increases significantly. When the rivulet attains its main flow form, the average liquid film thickness of the corrugated sheet is reduced owing to a large amount of liquid film distributed on the wave crest. As the  $Re$  further increases (to 560 and 620), the initial momentum of the liquid is sufficient to overcome the resistance of the corrugated sheet. In the process of falling film flow, it is easy to collide violently with ripples, causing the liquid to fall off the surface of the corrugated sheet, resulting in a certain mass loss and making the liquid volume significantly reduced. Therefore, the average liquid film thickness is also reduced. Figure 10 shows that when the  $Re$  is 500, the wetted area is the largest, at about  $0.022 \text{ m}^2$ . However, relative to the geometric area of the corrugated sheet, even if the  $Re$  reaches 500, the wetted area can only reach 20% of the surface area, and the overall wetting performance is still poor. Owing to the structure of the corrugated sheet, there is almost no liquid film coverage in the lower-left area. The liquid film thickness is unevenly distributed, which is not conducive to mass transfer. Therefore, the structure of the packing must be further optimized.

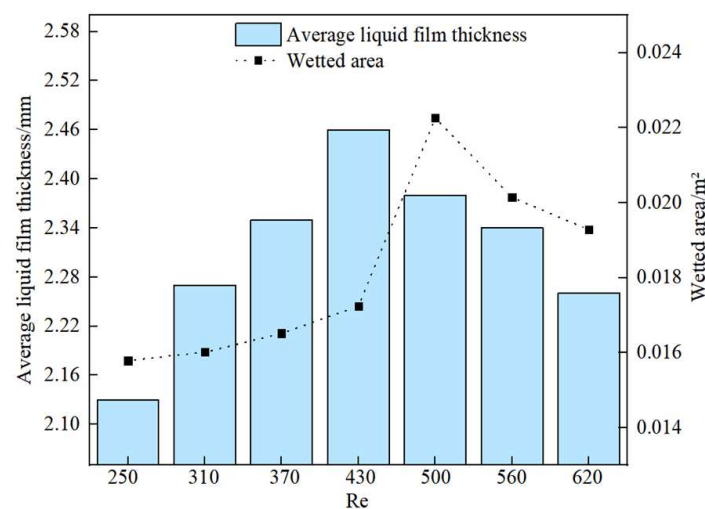


**Figure 10.** Average liquid film thickness and wetted area under different  $Re$ .

### 3.3. Triangular and Trapezoidal Corrugated Sheets

By changing the corrugation form from sinusoidal to triangular and trapezoidal, the effect of packing corrugation forms can be analyzed from the results shown in Figures 11 and 12.

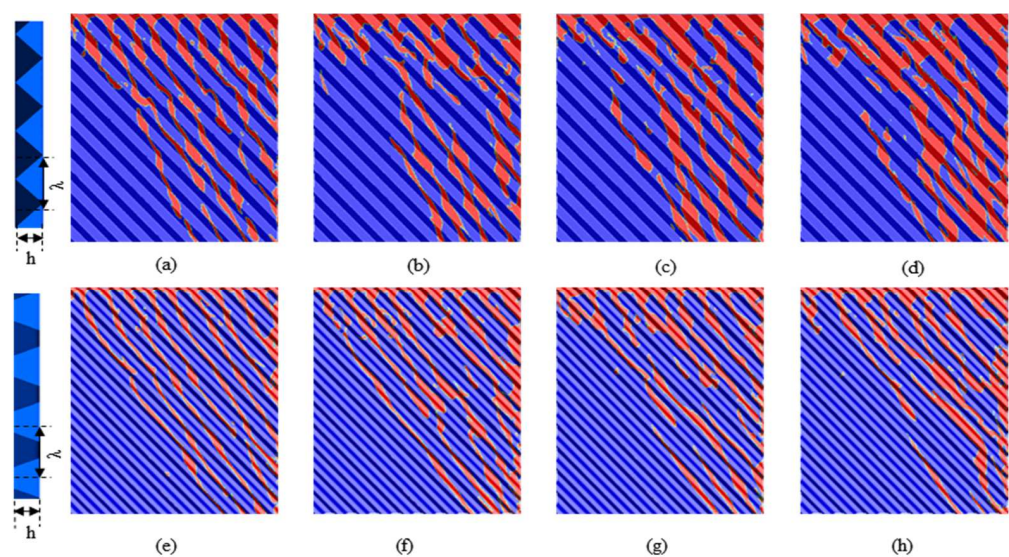


**Figure 11.** Wetting of the triangular and trapezoidal corrugated sheet under different  $Re$ : triangular—(a) 250, (b) 370, (c) 500, and (d) 620; trapezoidal—(e) 250, (f) 370, (g) 500, and (h) 620.

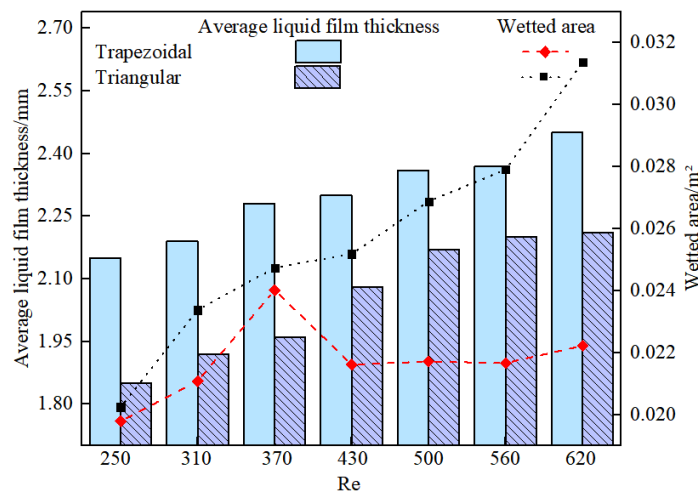


**Figure 12.** Average liquid film thickness and wetted area of the triangular and trapezoidal corrugated sheets under different Re.

Figure 11 shows the flow of triangular and trapezoidal corrugated sheets under different Re. It is clear that, compared with the sinusoidal corrugated sheet, the triangular structure has a less obstructive effect, which makes it easier for the liquid to cross the wave crest and flow down. Therefore, the triangular corrugated sheet does not have a Re for the transition from rivulet flow to groove flow. Basically, rivulet flow is the main one, which is conducive to the increase of the wetted area. As the Re increases, the rivulet width increases, causing the average liquid film thickness and wetted area to reach the peak at a maximum Re of 620. The trapezoidal corrugated sheet exhibits the same flow behavior as the triangular one, with a downward flow in the form of a rivulet under different Re. This means that, in the case of a low Re, the triangular and trapezoidal structures are better than sinusoidal corrugations, and a larger wetted area can be obtained.

Comparing Figures 10 and 12 reveals that, compared with the sinusoidal corrugated sheet data, the wetted area of the triangular corrugated sheet at the same Re is larger than that of the sinusoidal corrugated sheet. The trend of the average liquid film thickness is the opposite, even if the triangular corrugated sheet does not reach the peak value at Re = 500; its wetted area is still larger than that of the sinusoidal corrugated sheet. The triangular structure is more advantageous than the sinusoidal structure when the corrugation angle is  $45^\circ$ . The rivulet width of the trapezoidal corrugated sheet is considerably narrower than that of the triangular corrugated sheet, and the phenomenon of rivulet breaking is more serious. The data in Figure 12 are consistent with the aforementioned flow behavior of the liquid, and the wetted area does not show an increasing trend with the increase in Re; it basically remains unchanged. At an Re of 370, the only maximum wetted area that is different from that under the other Re appears. This may be because the trapezoidal structure causes part of the liquid to break outside the sheet, and 370 is the most suitable Re for the flow of the trapezoidal structure when the corrugation angle is  $45^\circ$ . Thus, the liquid can overcome the resistance and flow past the corrugation without breaking to the outside of the sheet owing to excessive amounts. At the same time, for the horizontal contrast between the triangular and trapezoidal corrugated sheets, the triangular sheet has a larger wetted area and a smaller average liquid film thickness, which is more conducive to mass transfer.

### 3.4. Effect of Corrugation Angle

In the previous simulation of the falling film flow over a corrugated sheet, the corrugation angle ( $\beta$ ) between the corrugation and the horizontal direction was fixed at  $45^\circ$ . Because the corrugation angle of the sheet significantly affects the wetted area, the influence of the corrugation angle was investigated by varying it from  $15^\circ$  to  $75^\circ$  for the three types

of corrugated sheets. The flow of liquid on the corrugated sheet is shown in Figure 13, and the characteristic parameters are shown in Figure 14.

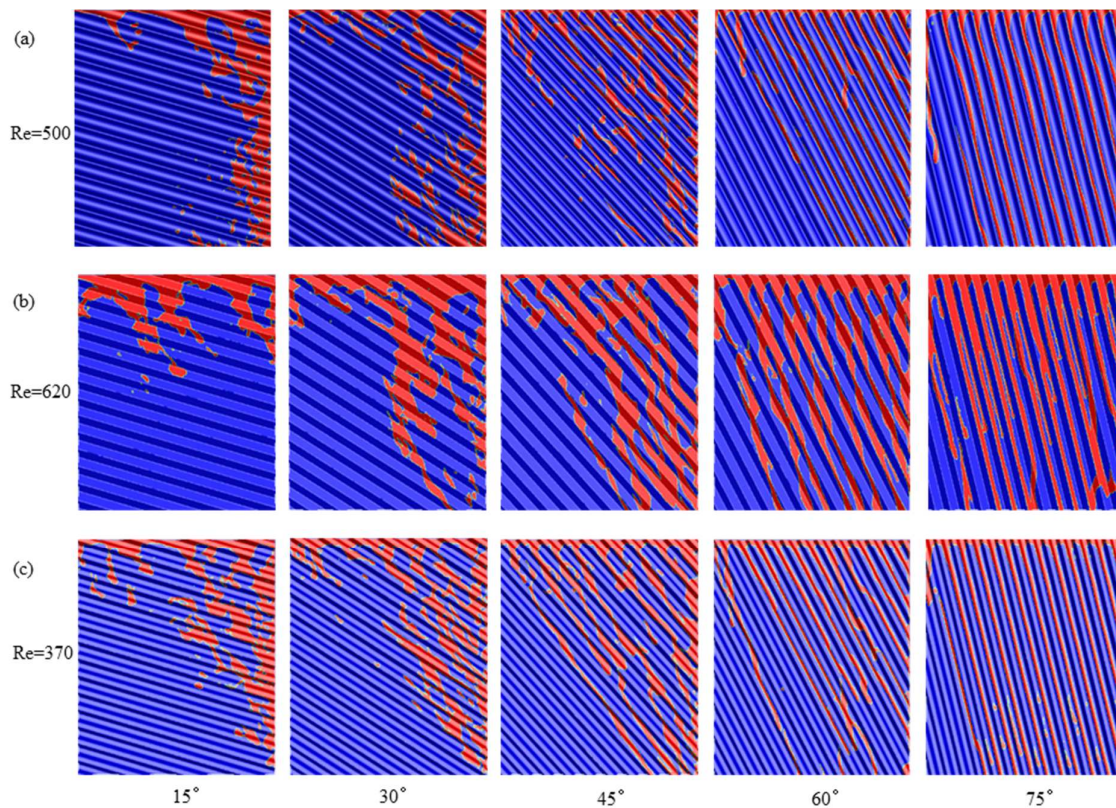


**Figure 13.** Effect of different corrugation angles of the three kinds of corrugated sheet on flow: (a) sinusoidal, (b) triangular, and (c) trapezoidal.

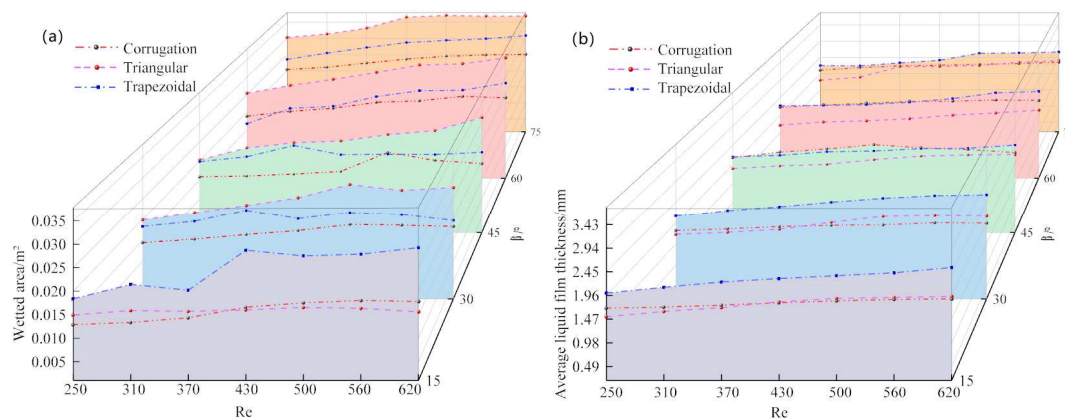


**Figure 14.** Two indicators against different Re and corrugation angles: (a) wetted area and (b) average liquid film thickness.

Figures 13 and 14 reflect the influence of the corrugation angle on the flow characteristics of the liquid falling film flow. For the sinusoidal corrugated sheet in Figure 13a, when  $\beta$  is  $15^\circ$  and  $30^\circ$ , the liquid flows in the form of a rivulet. The corrugated sheet has a small corrugation angle; hence, the breakage of the liquid film is mainly concentrated on the right side. The crest is covered with a large amount of liquid film because of the rivulet. When  $\beta$  is small, the resistance of the liquid falling film flow process is clearly greater, and the flow is not stable. When  $\beta$  is  $45^\circ$ ,  $60^\circ$ , and  $75^\circ$ , the lateral resistance of the corrugation gradually decreases, and the liquid easily forms a groove flow in the trough, so that the groove flow width and its wetted area increases with the increase in  $\beta$ , while the average

liquid film thickness gradually decreases. As shown in Figure 14a, the wetted area of the corrugated sheet is the largest when  $\beta$  is  $75^\circ$ ; the thinner liquid film in the trough is also conducive to mass transfer, as shown in Figure 14b. Although the shortening of the flow groove reduces the gas–liquid contact time, compared with the unstable flow conditions of the liquid at other corrugation angles and the existence of the dry zone at the lower left, a  $\beta$  of  $75^\circ$  is more conducive to improving the wetted area during the falling film flow process and reducing the average liquid film thickness.

According to the data in Figure 14, with the gradual increase in the corrugation angle, the wetted area increases, and the average liquid film thickness decreases for the triangular corrugated sheet. Combined with the liquid flow behavior shown in Figure 13b, the liquid flows downward in the form of a rivulet on the triangular corrugated sheet, and the negative correlation between the wetted surface and the average liquid film thickness shows that the triangular form does not accumulate a large amount of liquid in the troughs but promotes the downward flow of the liquid film to enhance the wetted area. For the trapezoidal corrugated sheet shown in Figure 13c, small fractures occur during the flow process at  $15^\circ$  and  $30^\circ$ , and they are concentrated on the right side of the sheet along the corrugation direction. The average liquid film thickness and wetted area show no obvious increasing trend with an increase in the angle but tend to be stable. This shows that the corrugation angle has little effect on the trapezoidal corrugated sheet. This may be because the trough channel of the trapezoidal corrugated sheet is relatively narrow, and the liquid flows down the trough, resulting in the same narrow rivulet width; it does not easily accumulate.

The aforementioned analysis demonstrates that the corrugation angle has different important effects on different structures. Considering the three variables of  $Re$ , corrugation angle, and corrugation form, triangular and trapezoidal corrugated sheets perform better than the commonly used sinusoidal corrugated sheets. The triangular structure has the highest wetted area, and the trapezoidal corrugated sheet has a lower average liquid film thickness. When the  $Re$  is changed, the best  $Re$  can increase the wetted area ratio of the sinusoidal corrugated sheet from 14.3% to 19.9%. By changing the corrugation angle, the wetted area can be increased to 18.4%. When the aforementioned two variables are changed at the same time, it can reach 22.1%. Although changing the two variables simultaneously does not produce a superimposed effect, it still improves. The wetted area of the trapezoidal corrugated sheet is as much as 28.9% of the surface area, and the wetted area of the triangular corrugated sheet is as much as 38.8%.

## 4. Discussion

### 4.1. Liquid Flow Behavior

In a previous study [37], the transient flow behavior of a rivulet on packing was investigated through simulation. In the intermediate period, the liquid had flow patterns, such as droplets, small rivulets, and rivulet ruptures, resulting in the maximum wetted area. When the flow reached the pseudo-steady state, a stable channel flow similar to the present results formed along the direction of the corrugations; the wetted area was also significantly reduced compared with the intermediate stage. In another study [7], the liquid flow behavior over packing under periodic boundary conditions was explored through simulation. Because of the setting of boundary conditions, there was no phenomenon where the liquid crossed the wave crest to form a large-scale rivulet phenomenon. However, the situation after its flow stability is similar to the results of this study. In the experiment of Li et al. [15], the liquid distribution on the Sic foam corrugated sheet was visualized using ultraviolet fluorescence technology. The results showed that a large amount of liquid was stored in the corrugated sheet trough, and only a small amount of liquid was distributed in the wave crest. The above research confirms the accuracy of the CFD simulation in this study.

However, it is worth noting that in all the above studies, the corrugated sheet had a large dry area, indicating that maximizing the wetting must be improved further. Therefore, improving the utilization rate of the packing should be the focus of future research.

#### 4.2. Optimal Corrugation Angle

For the corrugation angle, the research results of this study are different from those of previous research that analyzed the influence of corrugation angles of 35°, 45°, 50°, and 60° on the wetted area [37]. The wetted area changes nonmonotonously with an increase in the corrugation angle, and 45° is the best corrugation angle for enhancing the wetted area. However, owing to the control of the liquid inlet size, the liquid only flows in a single channel of the corrugated sheet, ignoring the interaction between different channels. In this study, a more extensive simulation (15°–75°) of the corrugated angle was performed, and the hydrodynamic characteristics of the three corrugated sheets at different corrugation angles are summarized in Table 4. It can be seen from the table that the wetted area increases with the increase of the corrugation angle. When the corrugated angle is 75°, the liquid flow is more stable, the nonwetted area at the lower-left corner of the corrugated sheet is reduced, and the wetted area reaches the maximum. This shows that a corrugation angle of 75° is more favorable. At the same time, the case where the corrugation angle is 90° was further simulated (as shown in Figure 15). Although structured packing is composed of multiple corrugated sheets that are staggered, meaning that 90° corrugated sheets cannot be used in actual projects, they can be used for investigation and comparison in simulations. The liquid flows in the troughs and the flow is more stable. Compared with other corrugation angles, the liquid flows in the trough with a stable flow, and the wetted area is larger, confirming the result obtained. An increase in the corrugation angle shortens the flow passage and reduces the gas–liquid contact time, indicating that a larger corrugation angle does not necessarily mean that the mass transfer performance is better [50], so further research is needed.

**Table 4.** Comparison of hydrodynamic characteristics under different corrugated sheet types.

Corrugated Sheet Type	Corrugation Angle $\beta$ (°)	Maximum Wetted Area (m <sup>2</sup> )	Hydrodynamic Characteristics
Sinusoidal corrugated sheet	15	0.018	Liquid builds up on the right and is badly fractured
	30	0.019	Rivulet flow occurs; extensive dry area
	45	0.022	A wide range of rivulet flow; irregularity
	60	0.024	Relatively stable groove flow
	75	0.025	Groove flow; the maximum wetted area
Triangular corrugated sheet	15	0.017	Serious fracture of the liquid film
	30	0.028	Unstable rivulet flow; small fractures
	45	0.031	A wide range of rivulet flow
	60	0.035	Relatively stable rivulet flow; larger width
	75	0.037	Rivulet flow; liquid film coverage is more uniform
Trapezoidal corrugated sheet	15	0.029	Rivulet flow phenomenon is weak; small fractures
	30	0.022	Serious liquid film breakage and detachment
	45	0.024	Relatively stable rivulet flow; smaller width
	60	0.028	Groove flow occurs; thick liquid film
	75	0.031	Steady groove flow; not conducive to mass transfer

#### 4.3. Limitations

Some scholars [51] have considered the influence of adjacent packing sheets on the wettability of corrugated sheets in their research. This was not considered in this study. In this study, only the flow of liquid on the corrugated sheet was considered, and the wetting condition of the corrugated sheet was analyzed through the two indices of average liquid film thickness and wetted area. The effect of the wetted area was determined, meaning that the larger the wetted area, the better the wetting performance of the corrugated sheet. The

average liquid film thickness was used to calculate the liquid hold-up, which is the amount of liquid that exists on the surface of the packing in the form of a liquid film or a rivulet [52]. Liquid hold-up is an important parameter that affects the pressure drop and mass transfer performance of the packed bed; however, this research is based on microscale simulation, and there is no quantitative criterion for the thickness of the liquid film to show that it is beneficial to the flow of liquid. The thickness of the liquid film in this study can only help to understand the accumulation of liquid over the corrugated sheet. The obstructive effect of gas to liquid is not considered because it does not affect the amount of retained liquid under the condition of the preinjection of water [53]. This simulation does not involve mass transfer, which is planned as the next research topic. Although the wetted area of the corrugated sheet can be increased by as much as 2.3 times by changing the corrugation form, the wetting performance of the corrugated sheet is still relatively poor. Similar to the triangular corrugated sheet of  $75^\circ$ , the highest wetted area only accounts for 39% of the surface area of the corrugated sheet; hence, more research is needed to improve the packing structure and enhance the wetting properties of the packing.

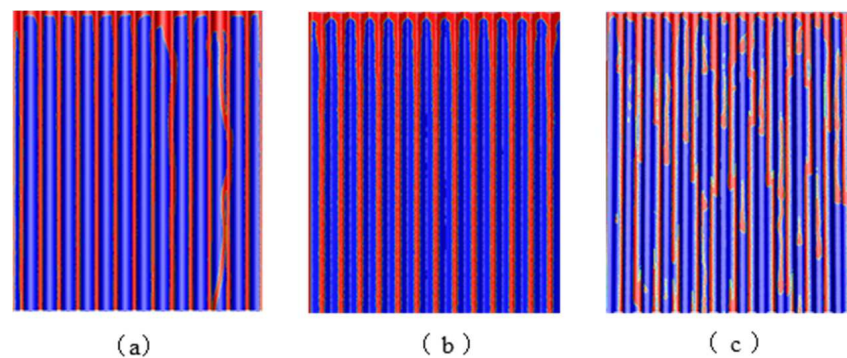


**Figure 15.** Wetting of the three corrugation forms when the corrugation angle is  $90^\circ$ : (a) sinusoidal, (b) triangular, and (c) trapezoidal.

## 5. Conclusions

Numerical simulations of the falling film flow in structured packings were performed to investigate the wetting behavior. Model validation was performed based on wetting simulations for the plate. Both the liquid film thickness and wetted area could be predicted well, both qualitatively and quantitatively. The main findings of this study are as follows.

- (1) The  $Re$  affects the wettability of the corrugated sheet by affecting the flow behavior of the liquid. For the sinusoidal corrugated sheet, the wetted area changes nonlinearly with the change in  $Re$ , and there is an optimal  $Re$  to maximize the wetted area. When the  $Re$  is small, the liquid flows on the corrugated sheet in the form of a groove flow. When the  $Re$  reaches 500, the rivulet becomes the main flow form, and the sinusoidal corrugated sheet exhibits the best wetting performance;
- (2) The corrugation form has a significant influence on wetting. In contrast to the change in the liquid flow form with  $Re$  on the sinusoidal corrugated sheet, the liquid on the triangular and trapezoidal corrugated sheets mainly flows in the form of rivulets. Hence, the two forms have a higher wetted area under the same  $Re$ . The wetted area of the triangular corrugated sheet is much higher than that of the remaining two forms with a thinner average liquid film thickness. However, regardless of the type of corrugation, the lower-left area is not wetted;
- (3) The corrugation angle,  $\beta$ , has a greater influence on the flow characteristics of the falling film, and the wetted area increases with the corrugation angle. When  $\beta$  is  $75^\circ$ , it is more conducive than other angle conditions to increasing the wetted area of the corrugated sheet and reducing the thickness of the liquid film for all three corrugation forms. Combining the influence of the corrugation form and the corrugation angle, it

is found that the triangular corrugated sheet has the best performance at a corrugation angle of 75°.

This work shows the influence of  $Re$  and  $\beta$  on the average liquid film thickness and wetted area from the perspective of flow. The wetting conditions of corrugated sheets with different corrugation forms were explored. The results can help in the design of an appropriate corrugated sheet structure. The optimization of heat and mass transfer performance should be considered in the future.

**Author Contributions:** Data curation, L.J.; Methodology, M.Z. and N.Z.; Software, J.L. (Junjie Liu); Writing—review & editing, J.L. (Junhua Liao) and P.X. All authors have read and agreed to the published version of the manuscript.

**Funding:** This research was funded by [name of the National Key R&D Program of China] grant number [2018YFC0705200] and The APC was funded by [Beijing University of Technology].

**Institutional Review Board Statement:** This study not involving humans or animals.

**Informed Consent Statement:** This study not involving humans or animals.

**Data Availability Statement:** This study did not report any data.

**Acknowledgments:** This work was supported by the National Key R&D Program of China (2018YFC0705200).

**Conflicts of Interest:** The authors declare no conflict of interest.

## References

1. Zhao, M.; Xue, P.; Liu, J.; Liao, J.; Guo, J. A review of removing SO<sub>2</sub> and NO<sub>x</sub> by wet scrubbing. *Sustain. Energy Technol. Assess.* **2021**, *47*, 101451. [[CrossRef](#)]
2. Xu, Y.Y.; Zhao, M.; Paschke, S.; Wozny, G. Detailed investigations of the countercurrent multiphase (gas-liquid and gas-liquid-liquid) flow behavior by three-dimensional computational fluid dynamics simulations. *Ind. Eng. Chem. Res.* **2014**, *53*, 7797–7809. [[CrossRef](#)]
3. Guo, J.M.; Zhao, M.J.; Xue, P.; Liang, X.; Fan, G.T.; Ding, B.H.; Liu, J.J.; Liu, J.P. New indicators for air quality and distribution characteristics of pollutants in China. *Build. Environ.* **2020**, *172*, 106723. [[CrossRef](#)]
4. Singh, R.K.; Bao, J.; Wang, C.; Fu, Y.; Xu, Z. Hydrodynamics of countercurrent flows in a structured packed column: Effects of initial wetting and dynamic contact angle. *Chem. Eng. J.* **2020**, *398*, 125548. [[CrossRef](#)]
5. Yang, D.; Zhu, H. Visualization of point mass transfer on structured packing surface. *Chem. Ind. Eng.* **2009**, *26*, 132–136.
6. Hu, J.G.; Liu, J.T.; Yuan, M.; Yu, J.G.; Dai, G.C. Hydrodynamics and mass transfer characteristics of a novel vertical-sheet structured packing. *Huagong Xuebao CIESC J.* **2014**, *65*, 116–122. [[CrossRef](#)]
7. Singh, R.K.; Galvin, J.E.; Sun, X. Multiphase flow studies for microscale hydrodynamics in the structured packed column. *Chem. Eng. J.* **2018**, *353*, 949–963. [[CrossRef](#)]
8. Wang, J.Q.; Ouyang, Y.; Li, W.L.; Esmaeili, A.; Xiang, Y.; Chen, J.F. CFD analysis of gas flow characteristics in a rotating packed bed with randomly arranged spherical packing. *Chem. Eng. J.* **2020**, *385*, 123812. [[CrossRef](#)]
9. Singh, R.K.; Galvin, J.E.; Sun, X. Three-dimensional simulation of rivulet and film flows over an inclined plate: Effects of solvent properties and contact angle. *Chem. Eng. Sci.* **2016**, *142*, 244–257. [[CrossRef](#)]
10. Wang, C.Y. Liquid film flowing slowly down a wavy incline. *AIChE J.* **1981**, *27*, 207–212. [[CrossRef](#)]
11. Wang, C.Y. Low Reynolds number film flow down a three-dimensional bumpy surface. *J. Fluids Eng. Trans. ASME* **2005**, *127*, 1122–1127. [[CrossRef](#)]
12. Argyriadi, K.; Vlachogiannis, M.; Bontozoglou, V. Experimental study of inclined film flow along periodic corrugations: The effect of wall steepness. *Phys. Fluids* **2006**, *18*, 3810. [[CrossRef](#)]
13. Zhang, H.; Yuan, X.; Kalbassi, M.A. Laser induced fluorescence technique for measuring liquid distribution in structured packing. *CIESC J.* **2014**, *65*, 3331–3339. [[CrossRef](#)]
14. Huang, Y.P.; Zhou, J.C.; Huang, J.J.; Lu, X.Y.; Liu, C.J.; Li, P.L.; Geng, Y.; Liu, H. Laser induced fluorescence technique for observing non-isothermal falling film flow on packing surface. *Chem. Ind. Eng. Prog.* **2016**, *35*, 3830–3835. [[CrossRef](#)]
15. Li, H.; Wang, F.Z.; Wang, C.C.; Gao, X.; Li, X.G. Liquid flow behavior study in SiC foam corrugated sheet using a novel ultraviolet fluorescence technique coupled with CFD simulation. *Chem. Eng. Sci.* **2015**, *123*, 341–349. [[CrossRef](#)]
16. Janzen, A.; Steube, J.; Aferka, S.; Kenig, E.Y.; Crine, M.; Marchot, P.; Toye, D. Investigation of liquid flow morphology inside a structured packing using X-ray tomography. *Chem. Eng. Sci.* **2013**, *102*, 451–460. [[CrossRef](#)]
17. Bradtmöller, C.; Janzen, A.; Crine, M.; Toye, D.; Kenig, E.; Scholl, S. Influence of Viscosity on Liquid Flow Inside Structured Packings. *Ind. Eng. Chem. Res.* **2015**, *54*, 2803–2815. [[CrossRef](#)]

18. Lu, X.K.; Bertei, A.; Finegan, D.P.; Tan, C.; Daemi, S.R.; Weaving, J.S.; O'Regan, K.B.; Heenan, T.M.M.; Hinds, G.; Kendrick, E.; et al. 3D microstructure design of lithium-ion battery electrodes assisted by X-ray nano-computed tomography and modelling. *Nat. Commun.* **2020**, *11*, 2079. [[CrossRef](#)]
19. Yang, Y.C.; Xiang, Y.; Chu, G.W.; Zou, H.K.; Sun, B.C.; Arowo, M.; Chen, J.F. CFD modeling of gas-liquid mass transfer process in a rotating packed bed. *Chem. Eng. J.* **2016**, *294*, 111–121. [[CrossRef](#)]
20. Zhang, W.; Xie, P.; Li, Y.X.; Teng, L.; Zhu, J.L. CFD analysis of the hydrodynamic characteristics in a rotating packed bed with multi-nozzles. *Chem. Eng. Process. Intensif.* **2020**, *158*, 108107. [[CrossRef](#)]
21. Cuce, E.; Sher, F.; Sadiq, H.; Cuce, P.M.; Guclu, T.; Besir, A.B. Sustainable ventilation strategies in buildings: CFD research. *Sustain. Energy Technol. Assess.* **2019**, *36*, 100540. [[CrossRef](#)]
22. Xue, P.; Ai, Z.T.; Cui, D.J.; Wang, W. A grey box modeling method for fast predicting buoyancy-driven natural ventilation rates through multi-opening atriums. *Sustainability* **2019**, *11*, 3239. [[CrossRef](#)]
23. Li, T.; Wang, G.; Zhou, H.; Ning, X.; Zhang, C. Numerical Simulation Study on the Effects of Co-Injection of Pulverized Coal and Hydrochar into the Blast Furnace. *Sustainability* **2022**, *14*, 4407. [[CrossRef](#)]
24. Shoeibi, S.; Kargarsharifabad, H.; Rahbar, N.; Ahmadi, G.; Safaei, M.R. Performance evaluation of a solar still using hybrid nanofluid glass cooling-CFD simulation and environmental analysis. *Sustain. Energy Technol. Assess.* **2022**, *49*, 101728. [[CrossRef](#)]
25. Yu, D.; Cao, D.P.; Li, Z.Z.; Li, Q.S. Experimental and CFD studies on the effects of surface texture on liquid thickness, wetted area and mass transfer in wave-like structured packings. *Chem. Eng. Res. Des.* **2018**, *129*, 170–181. [[CrossRef](#)]
26. Li, S.S.; Wang, Y.H.; Yang, Y.; Huang, Z.L.; Sun, J.Y.; Liao, Z.W.; Wang, J.D.; Yang, Y.R.; Du, B. Flow regime transition and liquid distribution in a 3D concurrent downflow three-phase moving bed. *Chem. Eng. J.* **2021**, *416*, 129174. [[CrossRef](#)]
27. Szulczewska, B.; Zbicinski, I.; Górak, A. Liquid Flow on Structured Packing: CFD Simulation and Experimental Study. *Chem. Eng. Technol.* **2003**, *26*, 580–584. [[CrossRef](#)]
28. Raynal, L.; Boyer, C.; Ballaguet, J.P. Liquid holdup and pressure drop determination in structured packing with CFD simulations. *Can. J. Chem. Eng.* **2004**, *82*, 871–879. [[CrossRef](#)]
29. Lu, X.; Xie, P.; Ingham, D.B.; Ma, L.; Pourkashanian, M. Modelling of CO<sub>2</sub> absorption in a rotating packed bed using an Eulerian porous media approach. *Chem. Eng. Sci.* **2019**, *199*, 302–318. [[CrossRef](#)]
30. Gu, F. CFD Simulations of the Local—Flow and Mass-Transfer in the Structured Packing. Ph.D. Thesis, Tianjin University, Tianjin, China, 2004.
31. Li, Q.S.; Wang, T.; Dai, C.N.; Lei, Z.G. Hydrodynamics of novel structured packings: An experimental and multi-scale CFD study. *Chem. Eng. Sci.* **2016**, *143*, 23–35. [[CrossRef](#)]
32. Hoffmann, A.; Ausner, I.; Repke, J.U.; Wozny, G. Fluid dynamics in multiphase distillation processes in packed towers. *Comput. Chem. Eng.* **2005**, *29*, 1433–1437. [[CrossRef](#)]
33. Ataki, A.; Bart, H.J. Experimental and CFD simulation study for the wetting of a structured packing element with liquids. *Chem. Eng. Technol.* **2006**, *29*, 336–347. [[CrossRef](#)]
34. Haroun, Y.; Raynal, L.; Alix, P. Prediction of effective area and liquid hold-up in structured packings by CFD. *Chem. Eng. Res. Des.* **2014**, *92*, 2247–2254. [[CrossRef](#)]
35. Shojaee, S.; Hosseini, S.H.; Rafati, A.; Ahmadi, G. Prediction of the effective area in structured packings by computational fluid dynamics. *Ind. Eng. Chem. Res.* **2011**, *50*, 10833–10842. [[CrossRef](#)]
36. Subramanian, K.; Wozny, G. Analysis of hydrodynamics of fluid flow on corrugated sheets of packing. *Int. J. Chem. Eng.* **2012**, *2012*, 838965. [[CrossRef](#)]
37. Singh, R.K.; Galvin, J.E.; Sun, X. Hydrodynamics of the rivulet flow over corrugated sheet used in structured packings. *Int. J. Greenh. Gas Control* **2017**, *64*, 87–98. [[CrossRef](#)]
38. Tan, L.Y.; Yuan, X.G.; Kalbassi, M.A. Computational fluid dynamics study of liquid distribution on structured packing surface. *Chem. Ind. Eng. Prog.* **2015**, *34*, 3221–3237. [[CrossRef](#)]
39. Ruan, X.D.; Liu, Z.H.; Qu, J.W. Study on application of PIV technique in two-phase flow measurement. *Zhejiang Daxue Xuebao Gongxue Ban J. Zhejiang Univ. Eng. Sci.* **2005**, *39*, 785–788.
40. *The State Bureau of Quality and Technical Supervision Evaluation and Expression of Uncertainty in Measurement JJJF 1059–1999*; National Institute of Metrology: Beijing, China, 1999.
41. Hirt, C.W.; Nichols, B.D. Volume of Fluid (VOF) Method for the Dynamics of Free Boundaries. *J. Comput. Phys.* **1981**, *39*, 201–225. [[CrossRef](#)]
42. Taha, T.; Cui, Z.F. Hydrodynamics of slug flow inside capillaries. *Chem. Eng. Sci.* **2004**, *59*, 1181–1190. [[CrossRef](#)]
43. Taha, T.; Cui, Z.F. CFD modelling of slug flow in vertical tubes. *Chem. Eng. Sci.* **2006**, *61*, 676–687. [[CrossRef](#)]
44. Taha, T.; Cui, Z.F. CFD modelling of slug flow inside square capillaries. *Chem. Eng. Sci.* **2006**, *61*, 665–675. [[CrossRef](#)]
45. Brackbill, J.U.; Kothe, D.B.; Zemach, C. A continuum method for modeling surface tension. *J. Comput. Phys.* **1992**, *100*, 335–354. [[CrossRef](#)]
46. Olujić, Ž.; Behrens, M.; Colli, L.; Paglianti, A. Predicting the efficiency of corrugated sheet structured packings with large specific surface area. *Chem. Biochem. Eng. Q.* **2004**, *18*, 89–96.
47. Paschke, S. Experimentelle Analyse ein- und Zweiphasiger Filmströmungen auf Glatten und Strukturierten Oberflächen. Ph.D. Thesis, Technische Universität Berlin, Berlin, Germany, 2011.

48. Nicolaiewsky, E.M.A.; Fair, J.R. Liquid flow over textured surfaces. 1. Contact angles. *Ind. Eng. Chem. Res.* **1999**, *38*, 284–291. [[CrossRef](#)]
49. ASHRAE. ASHRAE Guideline 14-2014, Measurement of Energy, Demand, and Water Savings. Available online: [www.ashrae.org/technology](http://www.ashrae.org/technology) (accessed on 5 October 2021).
50. Olujić, Ž.; Seibert, A.F.; Fair, J.R. Influence of corrugation geometry on the performance of structured packings: An experimental study. *Chem. Eng. Process. Process Intensif.* **2000**, *39*, 335–342. [[CrossRef](#)]
51. Dong, B.; Yuan, X.G.; Yu, K.T. Determination of liquid mass-transfer coefficients for the absorption of CO<sub>2</sub> in alkaline aqueous solutions in structured packing using numerical simulations. *Chem. Eng. Res. Des.* **2017**, *124*, 238–251. [[CrossRef](#)]
52. Hosseini, S.H.; Shojaee, S.; Ahmadi, G.; Zivdar, M. Computational fluid dynamics studies of dry and wet pressure drops in structured packings. *J. Ind. Eng. Chem.* **2012**, *18*, 1465–1473. [[CrossRef](#)]
53. Sebastia-Saez, D.; Gu, S.; Ranganathan, P.; Papadikis, K. Meso-scale CFD study of the pressure drop, liquid hold-up, interfacial area and mass transfer in structured packing materials. *Int. J. Greenh. Gas Control* **2015**, *42*, 388–399. [[CrossRef](#)]